

# A MOMENTUM-INTEGRAL METHOD TO CALCULATE WINDAGE LOSSES ON A ROTATING DRUM WITH SUPERPOSED FLOW

Haotian Tuo<sup>1</sup>, Peng Liu<sup>1</sup>, Shuiting Ding<sup>1</sup>, Tian Qiu<sup>1</sup>, Chuankai Liu<sup>1</sup>, Ronghui Cheng<sup>2,\*</sup>

<sup>1</sup>Research Institute of Aero-Engine, Beihang University, Beijing, 102206, China

<sup>2</sup>AECC Shenyang Engine Research Institute, Shenyang, 110015, China

#### **Abstract**

The evaluation of windage losses plays a significant role in the rapid analysis and design of the secondary air system in aero-engines. However, there is a lack of an effective model to calculate the windage losses of drums in aero-engines, since most of the empirical correlations derived from enclosed drums would be invalid when axial through-flow is supplied. Thus, an evaluation model based on the Von Karman-type momentum-integral method is presented to calculate the windage losses on the rotating drums with superposed flow. A 1/nth power law for the velocity profile is assumed, and the 1/7th power law is used for discussion purposes. Two cases are considered in this study: a rotating drum in an infinite space (Case 1) and a rotating drum in a rotor-stator cavity (Case 2). The results indicate that the moment coefficient exhibits a monotonic decline trend with an increase in rotational Reynolds number, inlet pre-swirl ratio, aspect ratio, and a reduction in Rossby number. Comparison results between the proposed theoretical model and CFD numerical method showed that the maximum discrepancy in the moment coefficients is less than 10% for Rossby numbers ranging from 0.1 to 1, rotational Reynolds numbers ranging from 0.4×10<sup>6</sup> to 2.5×10<sup>6</sup>, and inlet pre-swirl ratios ranging from 0 to 0.9. The relatively large discrepancy observed at low Rossby numbers is primarily attributed to the underestimation of the axial velocity.

Keywords: Windage; Drum; Superposed flow; Integral method; Moment coefficient.

## 1. Introduction

As an indispensable part of the aero-engine, the secondary air system (SAS) extracts air from the main flow for cooling and sealing to ensure safe engine operation. However, those airflows not directly contributing to engine thrust would result in a reduction in engine performance. Up to 6% of specific fuel consumption is caused by the use of this air during the overall operating cycle in a modern aero-engine [1]. Therefore, it is essential to analyze the transient performance of the SAS for multiple engine operating conditions. An important contributor to the influence is the windage loss. Windage is the effect of aerodynamic drag on the surface of a rotating system caused by fluid shear, and it is particularly prominent in high pressure environments. with the increasing demand for higher engine pressure ratios, higher rotational speed, and larger rotor size, the windage power losses are deteriorating, which has a direct impact on the turbine performance and engine efficiency. It is estimated that the windage power losses of the HPT front air delivery systems alone consume 0.83% of the overall HPT generating power [2].

The rotor-stator drum cavity is one of the typical components contributing to windage losses in the SAS. The structure of the rear drum cavity behind the compressor drive cone is illustrated in Figure 1. The rear drum is supplied with cooling air (also called the rotating drum with superposed flow) and windage occurs when fluid tangential velocity lags behind the rotor. For reasons of computational efficiency, the analysis and design of the SAS is typically conducted using a one-dimensional model. Therefore, it is necessary to establish a fast and high-fidelity model to calculate the windage losses on the drum with superposed flow. A common strategy used to study windage is to analyze the moment coefficient ( $C_m$ ) of the rotating walls, which quantifies the force required to overcome the frictional drag on the rotors.  $C_m$  is related to rotor size, rotational speed, density, and

dynamic viscosity of the air.  $C_m$  is usually expressed as either a power [3-5] or logarithmic [6-7] function of the rotational Reynolds number ( $Re_{\phi}$ ), and the empirical coefficients of which are often measured experimentally. Two different forms of  $C_m$  are derived from the different velocity profiles of the boundary layer. It is known that the velocity profile in the boundary layer of a fully developed turbulent flow obeys the logarithmic law, and the commonly used power law is an approximation of the logarithmic law for simplicity.

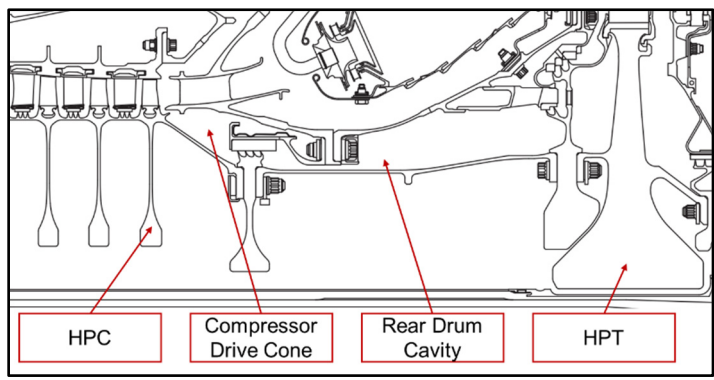


Figure 1 – Typical structure of the rear drum cavity in the secondary air system (CFM56-7)

A rotating drum in a quiescent infinite environment is referred to as a free drum. Theodorsen et al. [6] measured the torque of free drums rotating in air or water and expressed it as a function of rotational speed. Dorfman [8] utilized the mixing length theory in combination with the test results to acquire the  $C_m$  of a free drum, which aligns with the one obtained from Theodorsen's test [6]. Although the flow on a free drum differs from that in a drum cavity, the  $C_m$  of a free drum was used in SAS component modeling to evaluate engine performance in Ref. [1].

The flow within an enclosed rotating drum cavity is designated as Taylor-Couette flow. In 1923, Taylor [9] discovered that the type of instability is characterized by counter-rotating vortices spaced at regular intervals within the drum cavity when the rotating speed of the drum increased, which was named as Taylor vortices. Furthermore, Taylor defined a dimensionless parameter called Taylor number (*Ta*) and proposed that the critical value for the onset of vortices generation is 1708. Becker et al. [10] revealed that the flow in the cavity with inner drum rotation can be divided into four flow modes: laminar flow, laminar-plus-Taylor-vortices flow, turbulent flow, and turbulent-plus-Taylor-vortices flow. Subsequently, Andereck et al. [11] proposed a more detailed partition according to the different rotating speeds of the internal and external drums. To obtain a more accurate analysis of the flow pattern of Taylor vortices, large-eddy simulations were used by Schneider et al. [12]. Additionally, studies on Taylor-Couette flow encompass flow stability [13] and visualization tests [14].

A comprehensive overview of high Reynolds number Taylor-Couette studies is concluded by Grossmann et al. [15]. For enclosed drum cavities, the impact of clearance ratio  $s/R_o$  is also considered. Wendt's experiment results revealed that the  $C_m$  of an enclosed drum could be expressed as a power function of  $Re_\phi$  and the  $s/R_o$  [4]. Based on  $s/R_o$  and  $Re_\phi$ , the flow within the drum cavity was divided into four distinct partitions by Bilgen et al. [5] and  $C_m$  of each partition was determined from their experimental results. With the assumption that the tangential velocity in the middle of the annulus is half of the rotor speed, Yamada [7] derived an empirical correlation of Cm from using the logarithmic law velocity distributions. Subsequently, the accuracy of these windage models was verified experimentally [16] and numerically [17]. To assess the windage power losses of electric motors, the equations to calculate  $C_m$  of the enclosed drum above are widely used for their great precision, as reported in Ref. [18-19]. However, the empirical correlation of enclosed drums does not consider the influence of the air supplied, which varies considerably during the operating cycle of aero-engines. This results in a significant error.

Research on the drum with superposed flow has revealed that the flow pattern in the cavity is altered by the effect of the axial through flow. Gu et al. [20] found that Taylor vortices in the cavity are tilted in the axial direction with superposed flow. Using the incense and the laser light, Jeng et al. [21] obtained smoke flow visualization in rotating annulus. Their experimental results indicated that axial flow would suppress the onset of Taylor vortices, and Taylor vortices could not be observed

when the axial flow was large enough. In addition, Yamada [22] assumed that the effective velocity could be expressed as the root-mean-square (rms) of the mean axial velocity and tangential velocity, and derived an empirical coefficient for  $C_m$  by introducing the effective velocity. Based on numerical results, Hu et al. [23] established an empirical relationship between  $C_m$  and  $Re_{\phi}$ , as well as the radius ratio. The results indicated that  $C_m$  increases with the increasing through-flow. In an aero-engine, the flow in the annular between the HP shaft and LP shaft was experimentally investigated by Wu et al. [24]. However, the available empirical correlations consider a much lower  $Re_{\phi}$  than that of the rear drum cavity in the SAS, which would cause a large error in the evaluation of the windage on it.

An alternative approach to obtaining the  $C_m$  of the drum with superposed flow is the momentum integral method. A Von Karman's integral solution for turbulent flow on a rotating disk in a quiescent infinite environment (called a free disk) [3] is often used to provide rapid estimates of disk windage, supposing that the velocities satisfy the 1/7th power law based on the study of Blasius' experimental results. The integral solution was subsequently used to determine the windage of rotor-stator disk cavities [25]. However, only the thickness of the boundary layer of the drum with superposed flow was obtained through this methodology, which demonstrated a satisfactory agreement with their test results [26].

Therefore, this study proposes a theoretical solution to evaluate the  $C_m$  of a rotating drum with superposed flow, based on the momentum integral method. The numerical model was established by a verified computational fluid dynamics (CFD) approach. The effects of flow and geometrical parameters on  $C_m$  were discussed, as well as the discrepancy between theoretical and numerical methods. Finally, the boundary-layer velocity profiles were analyzed. This work offers novel insights into the windage evaluation of drums with superposed flow, thereby contributing to the refinement of the design and analysis of the SAS.

## 2. Theoretical Derivation

Figure 2 shows the velocity distributions in the boundary layer when a drum rotating in an infinite environment. The rotor is rotating around an axis at r=0 with a constant angular velocity  $\Omega$ , and the cylindrical coordinate system is used, with z,  $\phi$ , r representing the axial, tangential and radial component of coordinate direction, respectively. There is an superposed flow outside the drum, with the axial velocity  $V_{z,\infty}$  and tangential velocity  $V_{\phi,\infty}$ . L is the axial length of the drum and  $R_o$  is the radius of the rotor. When a static drum is deposited outside the rotor, the flow in the annulus has some resemblance to that in an infinite environment. Boundary layers form on both the rotor and stator surfaces, and the boundary-layer velocity distribution of rotor is similar to that in infinite space. Here,  $R_s$  is the radius of the stator, and s is the radial clearance between the rotor and stator. In this study, only the rotor's boundary layer will be analyzed, and the windage losses of drums will be solved with a momentum-integral method.

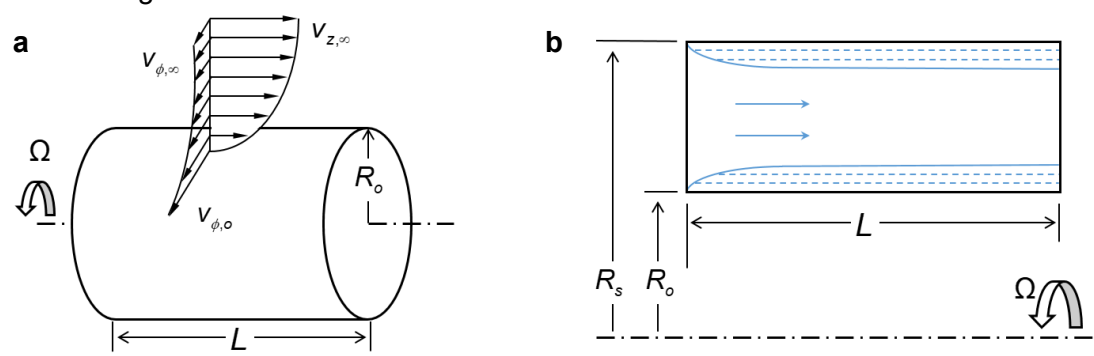


Figure 2 - Schematic diagram of the rotating drum with superposed flow. (a) the drum in infinite space. (b) the drum in rotor-stator cavity

The continuity and Navier-Stokes equations are established for a steady, incompressible and axisymmetric flow on the surface of a rotating drum. Therefore, the gradient of tangential velocity in the Navier-Stokes equations is neglected. It is hypothesized that the dynamic viscosity  $\mu$  and density  $\rho$  are constant. Consequently, the N-S equations can be written as

$$\frac{\partial \mathbf{v}_r}{\partial r} + \frac{\mathbf{v}_r}{r} + \frac{\partial \mathbf{v}_z}{\partial \mathbf{z}} = 0 \tag{1}$$

$$V_{r} \frac{\partial V_{\phi}}{\partial r} + V_{z} \frac{\partial V_{\phi}}{\partial z} + \frac{V_{r} V_{\phi}}{r} = \frac{1}{\rho} \frac{\partial T_{\phi}}{\partial r}$$
 (2)

$$V_{r} \frac{\partial V_{z}}{\partial r} + V_{z} \frac{\partial V_{z}}{\partial z} = -\frac{1}{\rho} \frac{\partial P}{\partial z} + \frac{1}{\rho} \frac{\partial T_{z}}{\partial r}$$
(3)

In these equations, the axial, tangential and radial components of velocity are denoted by  $v_z$ ,  $v_\phi$ , and  $v_r$ , respectively. P is the pressure of the flow.  $\rho$  is the density of the fluid.  $\tau_\phi$  and  $\tau_z$  are the tangential and radial components of shear stress. It is often convenient to rewrite Eq. (1) to Eq. (3) in the conservative form as

$$\frac{\partial (rv_r)}{\partial r} + \frac{\partial (rv_z)}{\partial z} = 0 \tag{4}$$

$$\frac{\partial (r^2 v_r v_\phi)}{\partial r} + \frac{\partial (r^2 v_z v_\phi)}{\partial z} = \frac{r^2}{\rho} \frac{\partial \tau_\phi}{\partial r}$$
 (5)

$$\frac{\partial (rv_r v_z)}{\partial r} + \frac{\partial (rv_z^2)}{\partial z} = -\frac{r}{\rho} \frac{\partial P}{\partial z} + \frac{r}{\rho} \frac{\partial \tau_z}{\partial r}$$
 (6)

Assuming that the thickness of the boundary layer is much smaller than the radius of the drum rotor and neglecting the axial pressure gradient of the flow near the drum, the momentum-integral equations can be obtained by integrating Eq. (4) to Eq. (6) between y = 0 and  $y = \delta$ . These can be written as

$$R_o V_{r,\infty} + R_o \frac{d}{dz} \int_0^{\delta} V_z dy = 0$$
 (7)

$$R_{o}^{2} V_{r,\infty} V_{\phi,\infty} + R_{o}^{2} \frac{d}{dz} \int_{0}^{\delta} V_{z} V_{\phi} dy = -\frac{R_{o}^{2}}{\rho} T_{\phi,o}$$
 (8)

$$R_o V_{r,\infty} V_{z,\infty} + R_o \frac{d}{dz} \int_0^{\delta} V_z^2 dy = -\frac{R_o}{\rho} \tau_{z,o}$$
(9)

In these equations,  $\delta$  represents the boundary layer thickness and y represents the normal distance from the wall. The 1/nth power law is used for this question, as given by

$$\frac{v}{u_{\tau}} = C_n \left(\frac{\rho u_{\tau} y}{\mu}\right)^{\frac{1}{n}} \tag{10}$$

where n is an arbitrary constant.  $C_n$  is a coefficient derived from test results. The friction velocity  $u_{\tau}$  is defined as follows:

$$u_r = (r_o/\rho)^{1/2}$$
 (11)

The axial and tangential velocity profiles of the flow in the vicinity of rotating drums can be expressed by [27]

$$\frac{V_{\phi}}{\Omega R_{o}} = 1 - \frac{V_{z}}{V_{z,\infty}} \tag{12}$$

Accordingly, in consideration of the tangential velocity outside the boundary,  $V_{\phi,\infty}$ , it is postulated that the radial and tangential velocity profiles are as follows:

$$V_z = V_{z,\infty} \left(\frac{y}{\delta}\right)^{\frac{1}{n}} = \alpha (1 - \beta) \Omega R_o \left(\frac{y}{\delta}\right)^{\frac{1}{n}}$$
(13)

$$V_{\phi} = V_{\phi,o} - (V_{\phi,o} - V_{\phi,\infty}) (\frac{y}{\delta})^{\frac{1}{n}} = \Omega R_{o} - (1 - \beta) \Omega R_{o} (\frac{y}{\delta})^{\frac{1}{n}}$$
(14)

where

$$\alpha = V_{z_{\infty}} / (V_{\phi_0} - V_{\phi_{\infty}}) \tag{15}$$

$$\beta = V_{doc} / (\Omega R_0) \tag{16}$$

In the equations,  $\alpha$  is the ratio of shear stresses and  $\beta$  is the swirl ratio, which is the tangential velocity ratio of the mainstream to the rotor. For the present, the equations are enclosed with the axial shear stress  $\tau_{z,o}$  and the tangential shear stress  $\tau_{z,o}$ , which can be expressed as

$$T_{z,o} = -\alpha T_{\phi,o} \tag{17}$$

$$\tau_{\phi,o} = -K_n \rho(v / \delta)^{\frac{2}{n+1}} [(1-\beta)\Omega R_o]^{\frac{2n}{n+1}} (1+\alpha^2)^{\frac{n-1}{2n+2}}$$
(18)

where  $K_n$  is a stress coefficient depending on n, given by

$$K_n = C^{-\frac{2n}{n+1}} \tag{19}$$

With the hypothesis that  $\alpha$  and  $\beta$  remain constant in the axial direction, Eq. (7) to Eq. (9) can be solved as

$$\frac{\delta}{z} = \left(K_n \frac{I_1}{I_2}\right)^{\frac{n+1}{n+3}} \alpha^{-\frac{n+1}{n+3}} (1 + \alpha^2)^{\frac{n-1}{2(n+3)}} \left[ (1 - \beta) Re_{\phi} \frac{z}{R_0} \right]^{-\frac{2}{n+3}}$$
(20)

where

$$I_1 = \frac{(n+1)(n+2)}{n} \tag{21}$$

$$I_2 = \frac{n+1}{n+3} \tag{22}$$

The rotational Reynolds number  $Re_{\phi}$  is defined as

$$Re_{_{\phi}} = \rho \Omega R_{_{0}}^{2} / \mu \tag{23}$$

Then, the windage torque M can be obtained by

$$M = -\int_{0}^{L} 2\pi R_{o}^{2} \tau_{\phi,o} dz = I_{3} \pi \rho \Omega^{2} R_{o}^{4} L (1 + \alpha^{2})^{\frac{n-1}{2(n+3)}} \alpha^{\frac{2}{n+3}} (1 - \beta)^{\frac{2(n+2)}{n+3}} (Re_{\phi} L / R_{o})^{-\frac{2}{n+3}}$$
(24)

where

$$I_3 = \frac{2(n+3)}{n+1} K_n^{\frac{n+1}{n+3}} (\frac{I_2}{I_1})^{\frac{2}{n+3}}$$
 (25)

The moment coefficient  $C_m$  is defined as

$$C_{m} = \frac{M}{\pi \rho \Omega^{2} R_{o}^{4} L} = \varepsilon_{m} R e_{\phi}^{-\frac{2}{n+3}}$$
(26)

where

$$\varepsilon_{m} = I_{3} Ro^{\frac{2}{n+3}} \left[1 + \left(\frac{Ro}{1-\beta}\right)^{2}\right]^{\frac{n-1}{2(n+3)}} \left(1 - \beta\right)^{\frac{2(n+1)}{n+3}} \left(\frac{L}{R_{o}}\right)^{-\frac{2}{n+3}}$$
(27)

Consequently,  $C_m$  is a function of Ro,  $Re_{\phi}$ ,  $\beta$  and aspect ratio  $L/R_o$ . The Rossby number is defined as

$$Ro = V_{z_{\infty}} / \Omega R_{o}$$
 (28)

The 1/7th power law is a frequently used approximation of the logarithmic law. When n = 7, the simplified expression for  $C_m$  is as follows:

$$C_m = 0.072Ro^{0.2} \left[1 + \left(\frac{Ro}{1-\beta}\right)^2\right]^{0.3} \left(1-\beta\right)^{1.6} \left(\frac{L}{R_o}\right)^{-0.2} Re_{\phi}^{-0.2}$$
 (29)

When the mainstream has no tangential velocity ( $\beta = 0$ ),  $C_m$  can be further simplified as follows:

$$C_m = 0.072Ro^{0.2}[1 + Ro^2]^{0.3} \left(\frac{L}{R_o}\right)^{-0.2} Re_{\phi}^{-0.2}$$
(30)

Accordingly, it is accessible to calculate the windage power loss by Eq. (31) once the Cm of the drum with superposed flow has been obtained.

$$P_{loss} = M\Omega = C_m(\pi \rho \Omega^3 R_o^4 L)$$
 (31)

In order to evaluate windage power loss, it is crucial to obtain  $C_m$  for a rotating drum when its geometry is determined. Therefore, the subsequent analysis will only focus on the dimensionless number  $C_m$  of the drum. Although the derivation above does not consider the effect of the stator's shear stress on the flow, the subsequent discussion indicates that the theoretical model is effective in evaluating the windage of the drum cavity with superposed flow, as the influence of the stator is limited.

## 3. Numerical Simulation

## 3.1 Model Establishment

A two-dimensional computational model was established in this paper for two cases, as shown in Figure 3. Case 1 depicts a rotating drum in an infinite space, which is not shrouded by a static drum. The mainstream has a specified axial velocity, while the tangential velocity is zero. Drawing on the free disk setup [28], the computational domain's radial dimension was set to five times the radius of the drum, and the axial dimensions of the left and right walls adjoining the drum were also set to five times the radius of the drum, respectively. To mitigate the edge effect of the computational domain, the left and right walls adjacent to the rotor were set as free-slip walls, with zero shear stress in each direction. Furthermore, the upper side of the domain was also set as a free-slip wall. The domain's left side served as a velocity inlet, characterized by a specified axial velocity and static temperature of 300 K. The domain's right side was set as a pressure outlet, with a zero gauge pressure setting. The reference pressure of the computational domain was set to 1 atm.

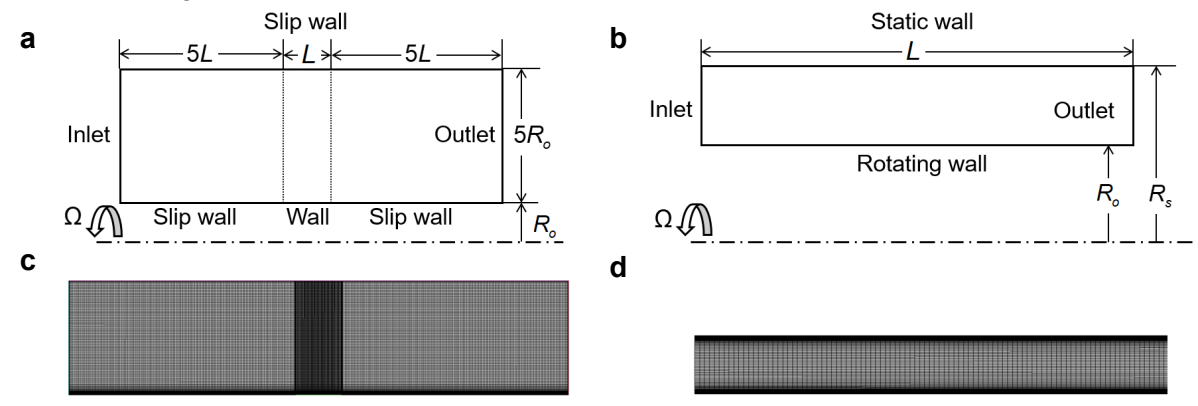


Figure 3 - Computational domain and mesh of CFD model. (a) Computation domain and boundary condition of the drum in an infinite space (Case 1). (b) Computation domain and boundary condition of the drum in rotor-stator cavity (Case 2). (c) Mesh in Case 1. (d) Mesh in Case 2.

In Case 2, the computational domain was defined as the annulus between the rotor and stator. The inlet parameters for case 2 can be calculated from the given  $Re_{\phi}$ , Ro, and  $\beta$ . The mass flow rate of the inlet can be calculated from Eq. (32) for a given Ro, provided that the axial variation of  $V_{z,\infty}$  is ignored. In fact, the change of  $V_{z,\infty}$  is negligible. Then, the total temperature of the inlet was acquired for a certain axial velocity, ensuring that the static temperature was 300K. Meanwhile, the axial and tangential components of the inlet velocity can be calculated for a given inlet swirl ratio  $\beta_{\rm in}$ . The reference pressure of the computational domain was set to 1 atm and the outlet pressure value was adjusted to ensure that the inlet gauge pressure was approximately zero. This method facilitates the analysis of the influence of a single factor on  $C_m$  while the other factors are held constant, with the inlet parameters used in the calculation of each dimensionless parameter.

$$\dot{m} = \rho V_{z,\infty} \pi(R_s^2 - R_o^2) = Ro \cdot \rho \Omega R_o \pi(R_s^2 - R_o^2)$$
 (32)

The simulation was carried out using the commercial program Ansys Fluent version 2020 R2.

In this study, a pressure-based solver was chosen and the SST k- $\omega$  turbulence model was used for the closure of equations. Without the application of near-wall treatment, this turbulence model allows us to analyze the boundary-layer velocity profile. The viscous heating option was enabled, and the pressure-velocity coupling scheme was Coupled. The least-squares cell-based gradient method was chosen for the evaluation of gradients and derivatives. All the equations were discretized in the second-order upwind format. The fluid was modeled as an ideal gas, and viscosity calculations were performed using the Sutherland equation. The model adopted a structured quadrilateral mesh generated by ICEM CFD, with local refinement near the wall to ensure that the maximum normalized wall distance y+ remained below 1. The first layer thickness of the boundary layer was 0.004mm, with a growth rate of 1.1.

In both Case 1 and Case 2, the values of L and  $R_o$  were 380mm, and 190mm, respectively, with  $L/R_o$  remaining constant at 2. Other aspect ratios were considered only in Section 4.2, with  $L/R_o$  = 1.5 and 1.0. In Case 2, the value of  $R_s$  was 202mm with  $s/R_o$  = 0.063, which is similar to the actual geometry of the rear drum with a static deflector in aero-engines. A numerical simulation was conducted for drums with a range of values for  $Re_\phi$  (1×10 $^6$  to 4×10 $^6$ ), Ro (0.1 to 1) and  $L/R_o$  (1, 1.5, 2), both in Case 1 and Case 2. In Addition, an analysis of  $\beta_{in}$  (0 to 0.9) was conducted in Case 2.

## 3.2 Model Validation

There is a paucity of available windage test data for the drum with superposed flow, whose  $Re_{\phi}$  is over  $10^6$ , which is close to the operating condition of aero-engines. Therefore, the validation of the CFD model was conducted with the experimental data of the enclosed drum investigated by Bilgen [5], which was in great agreement with the numerical results [16-17]. A set of experimental data of a drum that was geometrically similar to the model discussed in this paper was selected.  $R_s$  of the drum was 10.125 in with  $s/R_o = 0.08$ . A computational model similar to that of Case 2 was used, with the left and right sides of the computational domain set as free-slip walls. Otherwise, the non-slip setting would overestimate the windage because it would result in excessive localized shear forces at the left and right ends of the rotor. In fact, there was an axial gap between the rotor edge and the static wall of the test rig. Consequently, it is necessary to ignore the influence of the left and right sides of the stator on the rotor. The experimental data, with  $Re_{\phi}$  varying from  $1.2 \times 10^6$  to  $4 \times 10^6$ , was compared with the numerical results, as shown in Figure 4. Bilgen derived an empirical correlation from test results for drums with various  $s/R_o$  values, which was also plotted in Figure 4. The correlation is given by

$$C_m = 0.0325 \left(\frac{G}{R_o}\right)^{0.3} Re_{\phi}^{-0.2} \tag{33}$$

The computational results demonstrate that the SST  $k-\omega$  turbulence model exhibits sufficient precision for evaluating  $C_m$  of the enclosed drum. Within the selected  $Re_\phi$  range, the maximum error from the empirical correlation is 2%, and the maximum error from the experimental data is 9%.

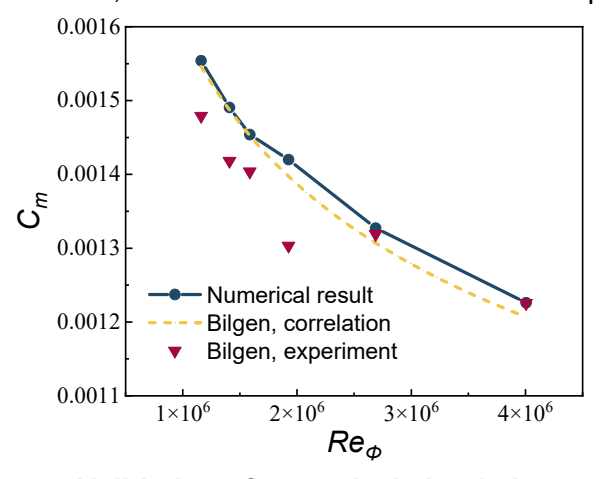


Figure 4 - Validation of numerical simulation results

In order to investigate the impact of grid size on simulation results, four sets of grids were used in this paper both in Case 1 and Case 2. In Case 1, the element numbers of the four girds were 6000,

37,500, 132,600, and 240,000, respectively. The discrepancy in  $C_m$  between the 132,600 and 240,000 grids was less than 0.02%. Similarly, four element numbers for grids were selected in Case 2: 30,000, 42,000, 62,400, and 129,000. The difference in  $C_m$  between the 62,400 and 129,000 grids was less than 0.05%. In consideration of the computational accuracy and time consumption, this paper selected a grid with 132,600 elements in Case 1 and the grid with 62,400 elements in Case 2.

## 4. Results and Discussion

This section is designed to analyze the influence of each single dimensionless parameter on  $C_m$ , including flow and geometrical parameters, which are discussed in detail in Sections 4.1 and 4.2, respectively. Furthermore, the differences between the theoretical and numerical results are discussed in Section 4.3, where both  $C_m$  and dimensionless velocity were analyzed.

# 4.1 Effects of Flow Parameters on Moment Coefficient

It is shown that  $C_m$  is affected by three principal dimensionless flow parameters:  $Re_{\phi}$ , Ro, and  $\beta_{\text{in}}$ , as indicated in Eq. (29). Ro represents the ratio of the axial velocity to the tangential velocity. As Ro increases, the axial inertia force increases and the through-flow effect gradually becomes dominant over the flow. Conversely, as Ro decreases, the through-flow capacity is weakened and the rotational effect gradually becomes dominant over the flow. The influence of flow parameters on  $C_m$  is shown in Figure 5. The results show that  $C_m$  rises monotonically as Ro increases in both Case 1 and Case 2 with an almost linear growth rate. This suggests that the enhancement of through-flow capacity intensifies the shear stress on the rotor's surface, resulting in a deterioration of windage losses. The theoretical results (Theo) are also displayed in Figure 5, which are in good agreement with the numerical results (Num). Furthermore, it is evident that the  $C_m$  in Case 2 is greater than that of Case 1, indicating that the existence of a stator increases the shear stress on the rotor's surface.

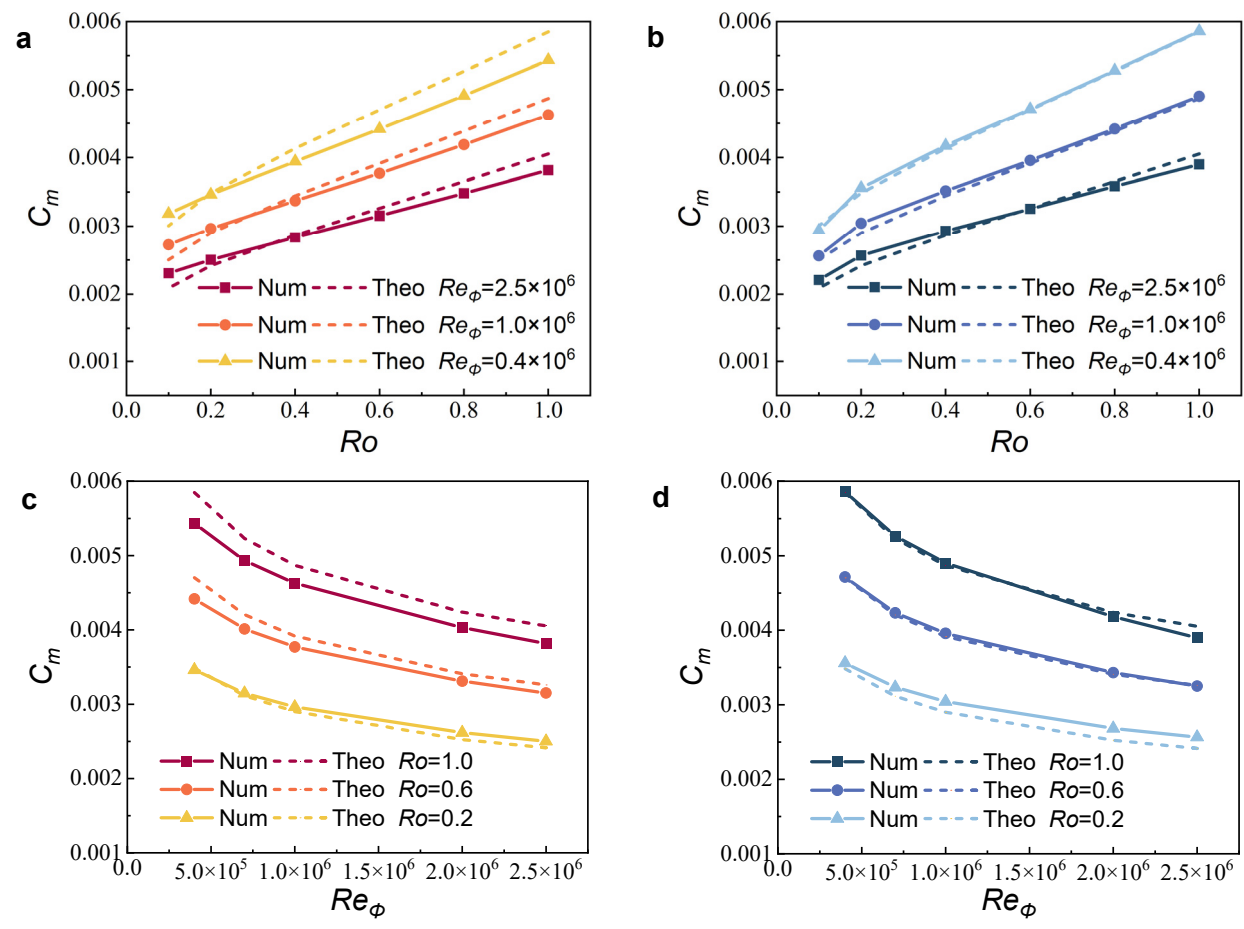


Figure 5 - Effect of flow parameters Ro and  $Re_{\phi}$  on  $C_m$ , with Ro ranging from 0.1 to 1 and  $Re_{\phi}$  ranging from 0.4×10<sup>6</sup> to 2.5×10<sup>6</sup> and  $L/R_o$  = 2. (a) Variation of  $C_m$  with Ro in Case 1. (b) Variation of  $C_m$  with Ro in Case 2. (c) Variation of  $C_m$  with  $Re_{\phi}$  in Case 1. (d) Variation of  $C_m$  with  $Re_{\phi}$  in Case 2.

 $Re_{\phi}$  is the ratio of the rotational inertia force to the viscous force of the air and the inertial force rises with  $Re_{\phi}$  increasing. While the viscous force cannot maintain the steady state, the flow becomes turbulent, which is commonly observed in SAS. Figure 5c and Figure 5d illustrate the effect of  $Re_{\phi}$  on  $C_m$  when Ro = 0.2, 0.6, and 1. The results show that  $C_m$  monotonically decreases as  $Re_{\phi}$  increases in both Case 1 and Case 2. However, the definition of  $C_m$  includes a quadratic term of rotational speed in the denominator, and the increase in Reynolds number has a nearly linear effect on the torque. Accordingly,  $C_m$  tends to decline with an increase in rotation speed. Nonetheless, the windage power loss, defined in Eq. (31), rises with an increase in rotation speed.

The influence of inlet pre-swirl is also considered in Case 2. In this paper, three cases with  $Re_{\phi}$  of 2.5×10<sup>6</sup> and Ro of 1.0, 0.6, and 0.2 are considered, with the inlet pre-swirl ratio varied from 0 to 0.9. As illustrated in Figure 6,  $C_m$  diminishes with the augmentation of  $\beta_{in}$ . when  $\beta$  approaches 1, the boundary-layer velocity gradient disappears, and  $C_m$  gradually approaches 0. Furthermore, the theoretical value calculated by Eq.(29), with the value of  $\beta$  taken as  $\beta_{in}$  for simplicity, is also displayed in Figure 6 using a dashed line, which is in good agreement with the CFD results. In fact,  $\beta$  varies slightly as a consequence of the progressive thickening of the boundary layer in the axial direction. Consequently, an alternative approach is to use the average value of  $\beta$ , though it is much harder to obtain.

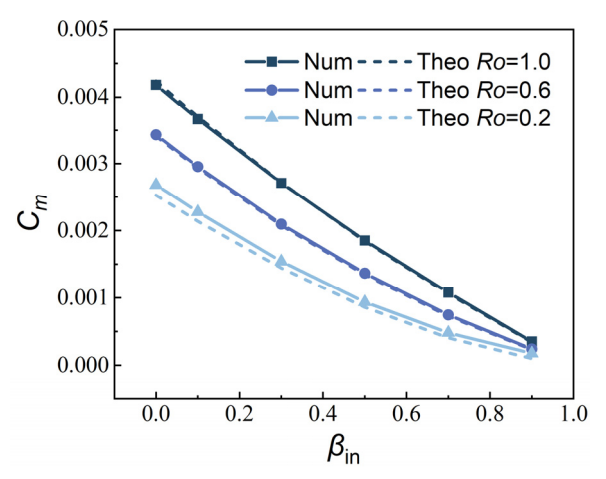


Figure 6 - Effect of flow Parameter  $\beta_{in}$  on  $C_m$  in Case 2 for  $Re_{\phi} = 2.5 \times 10^6$ ,  $L/R_o = 2$  and Ro = 0.2, 0.6, 1.0, respectively.

## 4.2 Effects of Geometrical Parameter on Moment Coefficient

In addition to the flow parameters discussed in Section 4.1 such as Ro,  $Re_{\phi}$ , and  $\beta$ , the influence of the geometrical parameter  $L/R_o$  derived from Eq.(29) is further analyzed in both Case 1 and Case 2. In this paper,  $L/R_o$  values of 1, 1.5, and 2 are considered respectively, which encompass the majority of the drum size ranges in the SAS. The results indicate that  $C_m$  drops slightly with the increase of  $L/R_o$ , as illustrated in Figure 7.

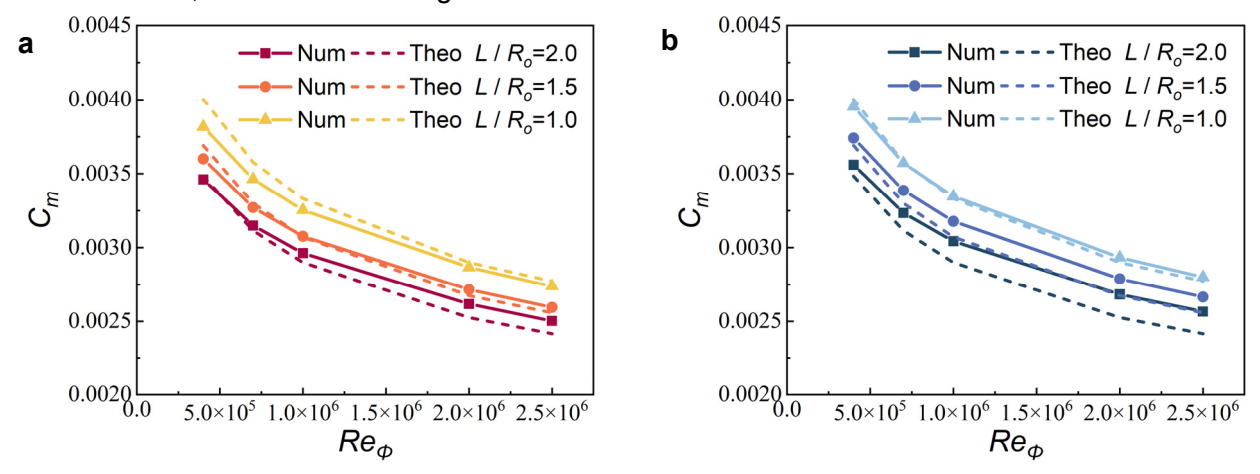


Figure 7 - Variation of  $C_m$  with  $Re_{\phi}$  where  $Re_{\phi}$  ranging from 0.4×10<sup>6</sup> to 2.5×10<sup>6</sup>,  $L/R_o$  ranging from 1 to 2, Ro = 0.2, and  $\beta_{in} = 0$ . (a) Case 1. (b) Case 2.

If we use the  $Re_{\phi} \cdot (L/R_o)$  as the abscissa in Figure 8, it can be observed that the influence of  $L/R_o$  is relatively minor when compared to the CFD results. The theoretical value of varied  $L/R_o$  is represented by a single dashed line, which is in good agreement with the numerical values of Ro = 0.2 and  $Re_{\phi}$  varied from  $0.4 \times 10^6$  to  $2.5 \times 10^6$ . it should be noted that there is another flow parameter  $R_s/R_o$  in Case 2. For a given inlet mass flow, varying  $R_s/R_o$  affects the axial velocity  $V_{z,\infty}$ , which in turn affects Ro. Consequently, the influence of  $R_s/R_o$  is not discussed separately.

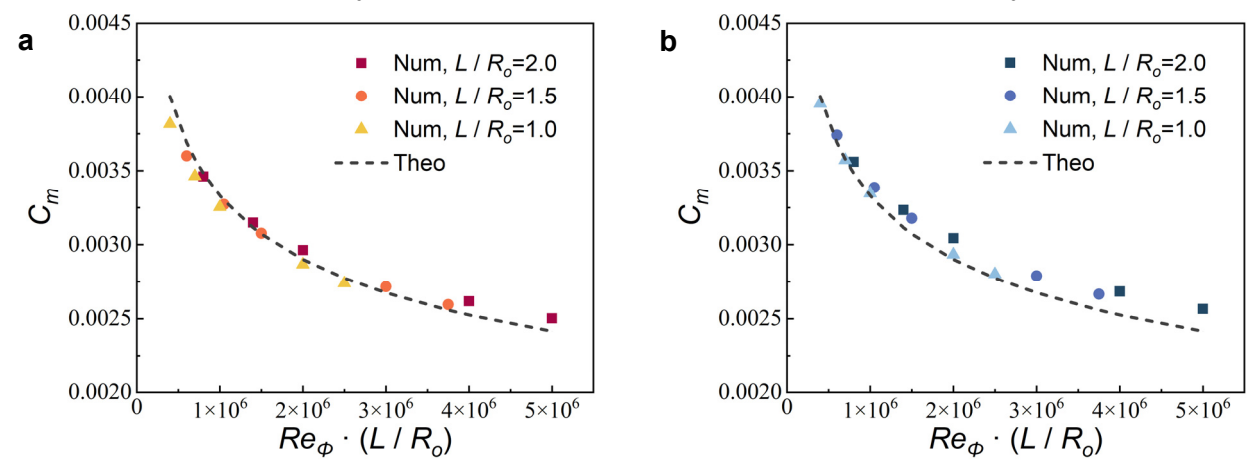


Figure 8 - Variation of  $C_m$  with  $Re_{\phi} \cdot (L/R_o)$  where  $Re_{\phi}$  ranging from 0.4×10<sup>6</sup> to 2.5×10<sup>6</sup>,  $L/R_o$  ranging from 1 to 2, Ro = 0.2, and  $\beta_{in} = 0$ . (a) Case 1. (b) Case 2.

# 4.3 Discrepancy of Moment Coefficient and Velocity Profile

The relative discrepancy between the  $C_m$  value obtained from the theoretical model and CFD methods is defined as  $\Delta C_m$ , which is defined by:

$$\Delta C_m = (C_{m.Theo} - C_{m.Num}) / C_{m.Num}$$
(34)

For the flow parameters, Ro and  $Re_{\phi}$  ranging from 0.1 to 1 and 0.4×10<sup>6</sup> to 2.5×10<sup>6</sup> respectively, the  $\Delta C_m$  of drums in Case 1 and Case 2 without inlet pre-swirl are both illustrated in Figure 9. In Case 1, the deviation curves are relatively simple, as Ro increases,  $\Delta C_m$  gradually changes from negative deviation to positive deviation, which indicates that the theoretical model gradually changes from underestimating windage to overestimating windage. Moreover,  $\Delta C_m$  changes slowly as Ro approaches 1, whereas  $\Delta C_m$  changes dramatically as Ro declines to 0.1. In Case 2, the deviation curves become more complex, exhibiting opposing trends for Ro varied from 0.1 to 0.2 and 0.2 to 1.0. Furthermore, the results suggest that  $\Delta C_m$  for the discussed situation in both Case 1 and Case 2 is less than 10%.

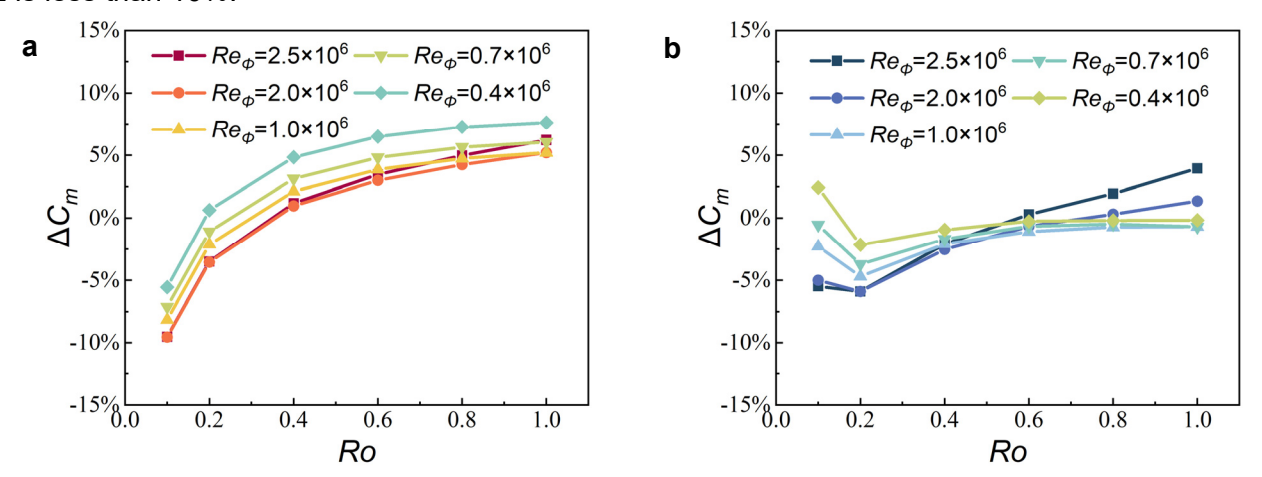


Figure 9 - Variation of  $\Delta C_m$  with Ro ranging from 0 to 0.1 and  $Re_{\phi}$  ranging from 0.4×10<sup>6</sup> to 2.5×10<sup>6</sup> for  $L/R_0$  = 0.2 and  $\beta_{in}$  = 0. (a) Case 1. (b) Case 2.

The effectiveness of this momentum-integral method is contingent upon a reasonable hypothesis of velocity profile in the boundary layer, which is generally accepted to satisfy the 1/7th law on disk surface. The applicability of the 1/7th power law on drum surface in Case 1 is discussed

as follows. The velocity is nondimensionalized with the wall rotating speed  $(\Omega \cdot R_o)$ , and the dimensionless velocity distributions within the boundary layer are plotted as shown in Figure 10. The normal distance from the wall, y is nondimensionalized with  $\delta$ , which is obtained from the location where the relative velocity is 99% of the mainstream velocity in CFD results. The dimensionless tangential and axial velocity distributions at different axial positions, z/L = 0.25, 0.5, and 0.75 are compared, respectively. The results demonstrate that they all comply with the 1/7th power law. Given that the velocity profile undergoes a little change in the axial direction, the velocity distributions at z/L = 0.5 are discussed for different flow parameters. With a fixed Ro = 0.2 and an increasing  $Re_{\phi}$ , both tangential and axial velocity distributions gradually become saturated due to the intensifying wall shear on the drum surface, as shown in Figure 10c and Figure 10d. Nevertheless, the overall change in the velocity profiles is relatively minor, and they are in good agreement with the theoretical value.

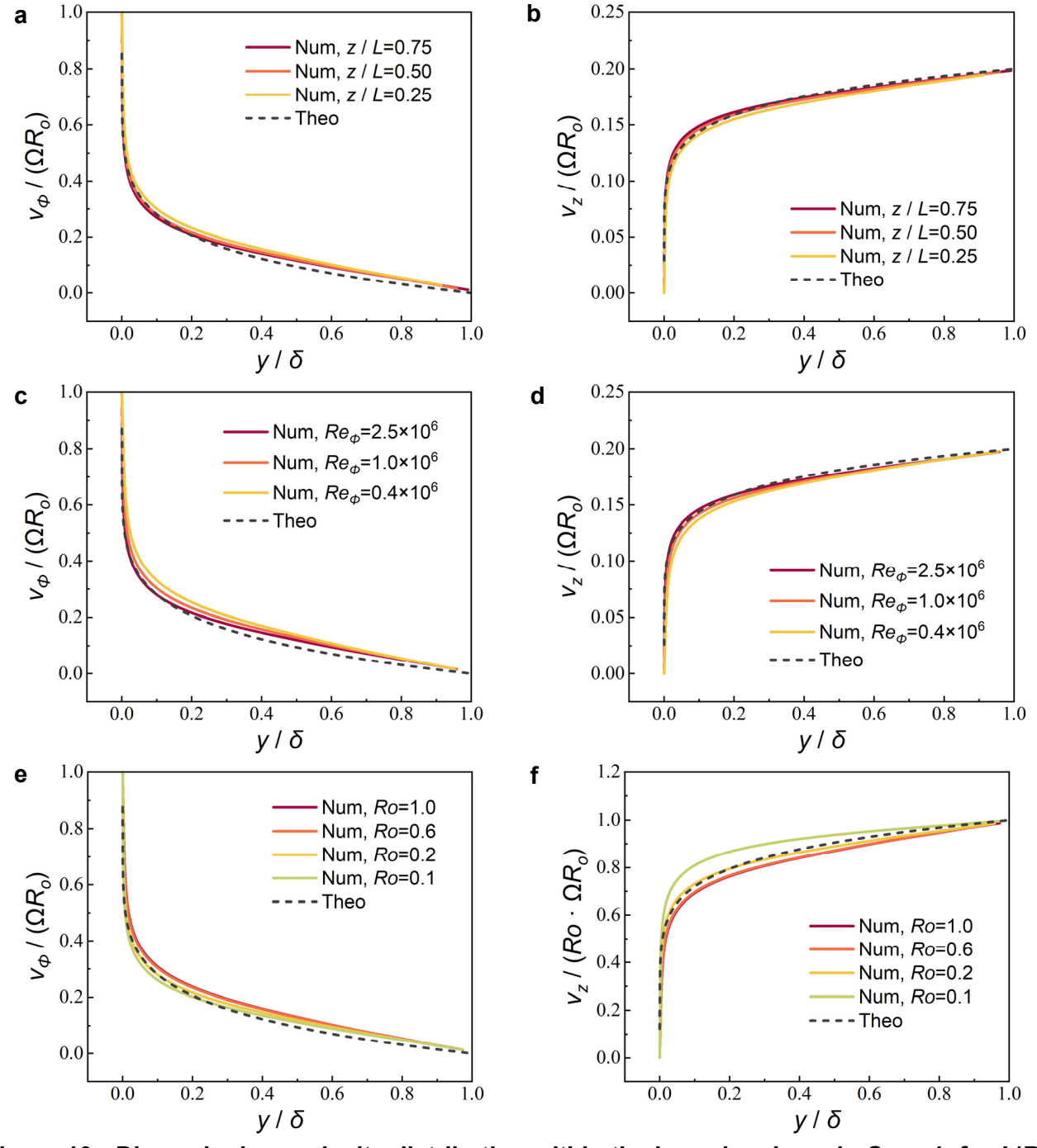


Figure 10 - Dimensionless velocity distribution within the boundary layer in Case 1, for  $L/R_o$  = 2 and  $\beta_{in}$  = 0. (a) Dimensionless tangential and (b) axial velocity distribution at different axial positions for Ro = 0.2 and  $Re_{\phi} = 2.5 \times 10^6$ . (c) Dimensionless tangential and (d) axial velocity distribution at z/L = 0.5 with varied  $Re_{\phi}$  and a fixed  $Re_{\phi}$  of 0.2. (e) Dimensionless tangential and (f) axial velocity distribution at z/L = 0.5 with varied  $Re_{\phi}$  and a fixed  $Re_{\phi}$  of  $2.5 \times 10^6$ .

In Case 1, the impact of Ro on the tangential velocity distribution is relatively minor, as shown in Figure 10e. In contrast, the axial velocity distribution varies sharply with a reduction in Ro, as shown in Figure 10f. The findings indicate that the theoretical model underestimates the axial velocity in the boundary layer, ultimately resulting in an underestimation of windage in Ro = 0.1. To eliminate the influence of Ro on theoretical value, the axial velocity is nondimensionalized by  $(Ro \cdot \Omega \cdot R_o)$ .

In Case 2, the effects of z/L,  $Re_{\phi}$  and Ro on the boundary layer velocity distribution are discussed without inlet pre-swirl, as illustrated in Figure 11. It is worth noting that for Case 2, the radial clearance s is used to normalize y instead of  $\delta$ , with y/s = 0 denoting the rotor wall and y/s = 1 denoting the stator wall. This is due to the fact that the velocity within the annulus undergoes a gradual change from the surface of the rotor to the stator. This subsequently leads to difficulties in extracting the thickness of the boundary layer from CFD results.

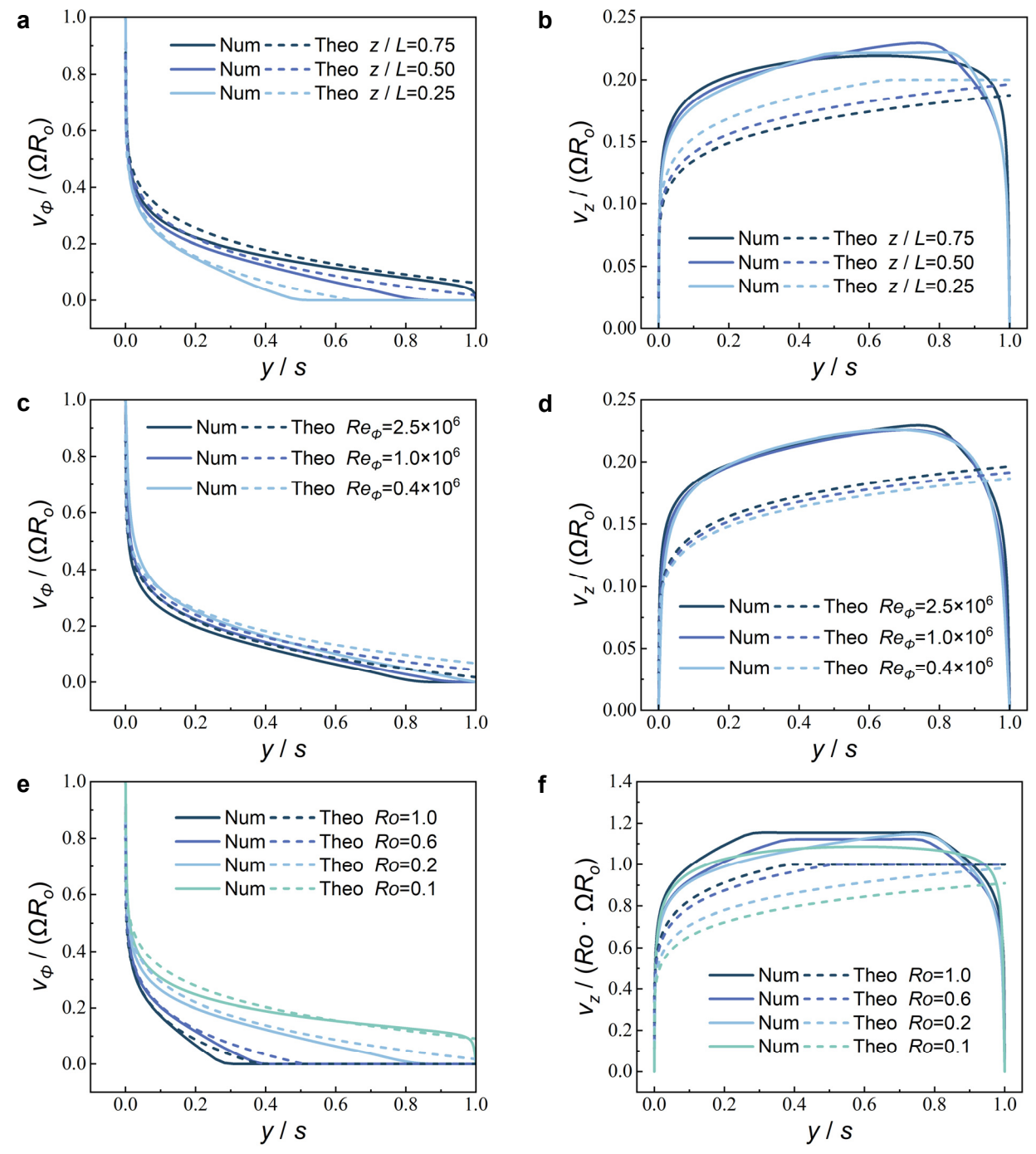


Figure 11 – Dimensionless velocity distribution within annulus in Case 2, for  $L/R_o$  = 2 and  $\beta_{in}$  = 0. (a) Dimensionless tangential and (b) axial velocity distribution at different axial positions for Ro = 0.2 and  $Re_{\phi}$  = 2.5×10<sup>6</sup>. (c) Dimensionless tangential and (d) axial velocity distribution at z/L = 0.5 with varied  $Re_{\phi}$  and a fixed Ro of 0.2. (e) Dimensionless tangential and (f) axial velocity distribution at z/L = 0.5 with varied Ro and a fixed  $Re_{\phi}$  of 2.5×10<sup>6</sup>.

In Case 2, the derivation of the velocity distribution within the drum annulus at various axial locations is shown in Figure 11a and Figure 11b, from which the theoretical value of  $\delta$  can be calculated by Eq. (20). The results suggest that the thickness of the rotor boundary layer increases and gradually fills the entire gap in the axial direction. Concurrently, the existence of the stator restricts the expansion of the rotor's boundary layer. Along the axial direction, the underestimation of the boundary-layer thinness is deteriorating. This consequently causes an underestimation of the axial velocity within the drum annulus in comparison to the CFD model. A further obvious finding is that the numerical  $\delta$  in Case 2 is thinner than that in Case 1, in comparison to the theoretical  $\delta$ . Given that the boundary-layer velocity distribution varies in the axial direction, the analysis of it at different axial locations is similar. For instance, velocity distribution within the annulus at position z/L = 0.5 is analyzed for different flow parameters  $Re_{\phi}$  and Ro. The influence of  $Re_{\phi}$  is discussed for Ro = 0.2 in Case 2. As Re<sub>0</sub> increases, the boundary layer thickness gradually becomes thinner, as shown in Figure 11c. The dimensionless tangential velocities generally agree with the theoretical model. However, the axial velocity distributions are relatively underestimated by the theoretical model, as shown in Figure 11d. Moreover, the effect of Ro on the velocity distributions is also discussed. For instance, when  $Re_{\phi}$  = 2.5×10<sup>6</sup>, the rotor's boundary layer gradually becomes thicker with the decreasing Ro, as shown in Figure 11e. In addition, the results suggest that the tangential velocity outside the boundary layer is no longer keeping zero for the small Ro value, such as 0.1. This improvement in the mainstream's tangential velocity weakens the windage and causes a decline in  $C_m$ . This phenomenon is caused by the merging of the boundary layers on the rotor and stator when Ro is less than 0.2. Figure 11f indicates that the axial velocity is underestimated by the theoretical model in Case 2, as well as in Case 1. The merging of the rotor's and stator's boundary layers results in a more intricate axial velocity distribution. Consequently, the utilization of a simplified velocity profile in the theoretical model will consequently result in a greater derivation.

## 5. Conclusions

This paper considers two common cases for a rotating drum with superposed flow: a rotating drum in an infinite space (Case 1) and a rotating drum in the rotor-stator cavity (Case 2). The influence of flow parameters  $Re_{\phi}$ , Ro,  $\beta_{in}$ , and the geometrical parameter  $L/R_o$  on  $C_m$  are discussed. The discrepancy between the theoretical model based on the momentum-integral method and the CFD model is analyzed. The main conclusions are as follows:

- (1) In both cases, the results indicate that  $C_m$  exhibits a monotonic decline trend with an increase in  $Re_{\phi}$ ,  $L/R_o$ , and a reduction in Ro. Moreover, an increasing  $\beta_{in}$  is effective in reducing  $C_m$ , with the consequence that  $C_m$  declines to zero with  $\beta_{in}$  rising to 1, as shown in Case 2.
- (2) As an alternative approximation of the logarithmic law, the 1/7th law is effective in estimating the tangential and axial velocity distribution in the drum's boundary layer, particularly in Case 1. However, the theoretical method underestimates the axial velocity in Case 2, due to the influence of shear stress on the stator.
- (3) The  $C_m$  value calculated by the theoretical model is in good agreement with the numerical results. The discrepancy  $\Delta C_m$  is less than 10% under the simulation conditions discussed in this study, with  $Re_\phi$  varied from  $0.4\times10^6$  to  $2.5\times10^6$ , Ro from 0.1 to 1,  $L/R_o$  from 1 to 2, and  $\beta_{in}$  from 0 to 0.9. As Ro decreases to zero, the effect of the through-flow gradually diminishes, while the effect of rotation becomes dominant. The simplified hypothesis of the axial velocity distribution would cause an additional deviation of the windage.

## 6. Nomenclature

C<sub>m</sub> moment coefficient
 C<sub>n</sub> coefficient of the velocity profile
 K<sub>n</sub> stress coefficient up to n
 L drum length (m)
 M windage torque (N·m)
 m mass flow rate of inlet (kg·s<sup>-1</sup>)
 n arbitrary constant of the velocity profile

P pressure (N·m<sup>-2</sup>)

 $P_{loss}$  windage power loss (N·m·s<sup>-1</sup>)

R radius of the drum (m)

*Re*<sub>φ</sub> rotational Reynolds number

Ro Rossby number

s radial clearance between the rotor and stator (m)

TaTaylor number $u_{\scriptscriptstyle T}$ friction velocity

 $v_z$ ,  $v_\phi$ ,  $v_r$  axial, tangential, radial components of velocity within the boudary layer (m·s<sup>-1</sup>, m·s<sup>-1</sup>

<sup>1</sup>, m·s<sup>-1</sup>)

 $V_z$ ,  $V_\phi$ ,  $V_r$  axial, tangential, radial components of velocity outside the boudary layer (m·s<sup>-1</sup>,

 $m \cdot s^{-1}, m \cdot s^{-1}$ 

y normal distance from the rotor (m)

y+ normalized wall distance

z,  $\phi$ , r axial, tangential, radial coordinates (m, rad, m)

## **Greek letters**

α ratio of axial and tangential shear stresses

 $\beta$  swirl ratio, a tangential velocity ratio of the mainstream to rotor

Δ relative discrepancy between the theoretical model and numerical model

 $\varepsilon_m$  influence factor of the moment coefficient

 $\mu$  dynamic viscosity (N·s·m<sup>-2</sup>)

ρ density (kg·m<sup>-3</sup>)

 $\tau_z$ ,  $\tau_\phi$ ,  $\tau_r$  axial, tangential, radial components of shear stress (N·m<sup>-2</sup>)

Ω angular velocity (rad·s<sup>-1</sup>)

# **Subscripts**

in inlet

o refers to rotor s refers to stator

z, φ, r axial, tangential, radial direction
 ∞ flow outside the boundary layer

## 7. Contact Author Email Address

Ronghui Cheng: rhcheng\_gte@sina.com
Or Haotian Tuo: tuohaotian@buaa.edu.cn

## 8. Copyright Statement

The authors confirm that they, and/or their company or organization, hold copyright on all of the original material included in this paper. The authors also confirm that they have obtained permission, from the copyright holder of any third party material included in this paper, to publish it as part of their paper. The authors confirm that they give permission, or have obtained permission from the copyright holder of this paper, for the publication and distribution of this paper as part of the ICAS proceedings or as individual off-prints from the proceedings.

## References

- [1] Alexiou A, Mathioudakis K. Secondary Air System Component Modeling for Engine Performance Simulations. *Journal of Engineering for Gas Turbines and Power*, 3, 131, 2009.
- [2] Villazón J M R, Wildow T and Benton R. Impact of the secondary air system design parameters on the calculation of turbine discs windage. ASME Turbo Expo Turbine Technical Conference & Exposition, 2014.

- [3] Kármán T V. Über laminare und turbulente Reibung. ZAMM Journal of Applied Mathematics and Mechanics/Zeitschrift für Angewandte Mathematik und Mechanik, 1, 4, 233-52, 1921.
- [4] Wendt F. Turbulente Strömungen zwischen zwei rotierenden konaxialen Zylindern. *Ingenieur-Archiv*, 4, 6, 577-95,1933.
- [5] Bilgen E, Boulos R. Functional Dependence of Torque Coefficient of Coaxial Cylinders on Gap Width and Reynolds Numbers. *Journal of Fluids Engineering*, 95, 1, 122-6, 1973.
- [6] Theodorsen T, Regier A. Experiments on drag of revolving disks, cylinders, and streamline rods at high speeds. *Nat. Advisory Comm. Aeronaut, Report*, 793, 367, 1944.
- [7] Yamada Y. Torque resistance of a flow between rotating co-axial cylinders having axial flow. *Bulletin of JSME*, 5, 20, 634-42, 1962.
- [8] Dorfman L A, Kemmer N. Hydrodynamic resistance and the heat loss of rotating solids, 1963.
- [9] Taylor, G I. VIII. Stability of a viscous liquid contained between two rotating cylinders. *Philosophical Transactions of the Royal Society of London. Series A, Containing Papers of a Mathematical or Physical Character*, 223, 605-615, 289-343, 1923.
- [10]Becker K M, Kaye J. Measurements of Diabatic Flow in an Annulus With an Inner Rotating Cylinder. *Journal of Heat Transfer*, 84, 2, 97-104, 1962.
- [11] Andereck C D, Liu S and Swinney H L. Flow regimes in a circular Couette system with independently rotating cylinders. *Journal of fluid mechanics*, 164, 155-83, 1986.
- [12]Schneider M, Younis B and Weigand B. Large-eddy simulations of flow and heat transfer in heated concentric annulus with inner cylinder rotation. *International Journal of Heat and Mass Transfer*, 114, 1248-62, 2017.
- [13] Chandrasekhar S. The stability of spiral flow between rotating cylinders. *Proceedings of the Royal Society of London Series A Mathematical and Physical Sciences*, 265,1321, 188-97, 1962.
- [14]Ramesh P, Bharadwaj S and Alam M. Suspension Taylor-Couette flow: Co-existence of stationary and travelling waves, and the characteristics of Taylor vortices and spirals. *Journal of Fluid Mechanics*, 870, 901-40, 2019.
- [15] Grossmann S, Lohse D and Sun C. High-Reynolds number Taylor-Couette turbulence. *Annual review of fluid mechanics*, 48, 53-80, 2016.
- [16]Wild P, Djilali N and Vickers G. Experimental and computational assessment of windage losses in rotating machinery. *Journal of Fluids Engineering*, 118, 1, 116-122, 1996.
- [17]Deng Q, Hu L and Zhao Y. Windage Loss Model Verification and Flow Characteristic Analysis in Shaft-Type Gap. *Hsi An Chiao Tung Ta Hsueh*, 56, 5, 54-63, 2022.
- [18]Kiyota K, Kakishima T and Chiba A. Estimation and comparison of the windage loss of a 60 kW Switched Reluctance Motor for hybrid electric vehicles. *IEEE*, 2014.
- [19]Rosset K, Schiffmann J. Extended windage loss models for gas bearing supported spindles operated in dense gases. *Journal of Engineering for Gas Turbines and Power*, 142, 6, 2020.
- [20]Gu Z, Fahidy T. Visualization of flow patterns in axial flow between horizontal coaxial rotating cylinders. *The Canadian Journal of Chemical Engineering*, 63, 1, 14-21, 1985.
- [21] Jeng T M, Tzeng S C and Chang H L. Flow visualization in an annulus between co-axis rotating cylinders with a circular jet on stationary outer cylinder. *International communications in heat and mass transfer*, 39, 8, 1119-24, 2012.
- [22]Yamada Y. Resistance of a flow through an annulus with an inner rotating cylinder. *Bulletin of JSME*, 5, 18, 302-10, 1962.
- [23]Hu L, Deng Q, Liu Z, et al. Action mechanism of axial flow on windage loss in open shaft-type gap with CO2. *Energy Sci Eng*, 2023.
- [24]Wu H W, Ding S T, Yuan Y X,et al.Thermal state experimental research on flow in an annular composed of two co-axial cylinders rotating independently. *Tuijin Jishu/Journal of Propulsion Technology*, 22, 5, 397-399, 2001.
- [25]Owen J M. An Approximate Solution for the Flow Between a Rotating and a Stationary Disk. *Journal of Turbomachinery*, 111, 3, 323-32, 1989.
- [26] Furuya Y, Nakamura I. Velocity profiles in the skewed boundary layers on some rotating bodies in axial flow. *Journal of Applied Mechanics*, *Transactions ASME*, 37, 1, 17-24, 1970.
- [27] Child P R N. Rotating Flow. Burlington, US: Butter-worth-Heinemann, 2011.
- [28] Chang R, Liu G W, Chen Q, et al. Numerical Study on the Similarity of Flow and Heat Transfer on a High-Speed Rotating Free Disk. *Kung Cheng Je Wu Li Hsueh Pao*, 41, 10, 2561-70, 2020.